PHYSICAL REVIEW B **105**, 115433 (2022)

Moiré-induced band-gap opening in one-dimensional superlattices of carbon nanotubes on hexagonal boron nitride

Xianliang Zhou,[1,*] Jingxu Xie,[2,*] Gengpu Li,[1,*] Jianing Zhang,[1] Minggang Xia,[2] Weidong Luo,[1,3,†] and Zhiwen Shi[1,‡]
[1]*Key Laboratory of Artificial Structures and Quantum Control (Ministry of Education), Shenyang National Laboratory for Materials Science, School of Physics and Astronomy, Shanghai Jiao Tong University, Shanghai 200240, China*
[2]*Department of Applied Physics, School of Physics, Xi'an Jiaotong University, 710049, China*
[3]*Institute of Natural Sciences, Shanghai Jiao Tong University, Shanghai 200240, China*

(Received 21 December 2021; revised 20 March 2022; accepted 22 March 2022; published 30 March 2022)

Recently, two-dimensional (2D) moiré superlattices have been extensively studied, and many interesting physical phenomena have been observed. However, their one-dimensional (1D) counterpart—1D moiré superlattices—have been rarely explored yet. Here, we performed theoretical calculations of low-energy bands of 1D moiré superlattices of single-walled carbon nanotubes (CNTs) on hexagonal boron nitride (hBN) using a newly developed low-energy effective continuum model for 1D superlattices. We observed moiré-induced opening of small band gaps ranging from a few meV to a few tens of meV, which depends sensitively on the CNT chirality. The observed band-gap opening can be well understood by considering the coupling of electronic states between CNTs and the hBN using the effective continuum model. The results have been confirmed by the density functional theory calculations.

DOI: 10.1103/PhysRevB.105.115433

I. INTRODUCTION

Two-dimensional (2D) moiré superlattices have attracted tremendous research interest due to their intriguing physical properties. In 2D moiré superlattices, it has been found that the moiré superlattice potential strongly modifies the electronic band structure at the low-energy region [1,2], and at certain moiré periods, a flat band emerges [3–6], which offers a new platform to study electronic strongly correlated systems. Many interesting physical phenomena, such as Wigner crystals, Mott insulators, and superconductivity, have already been observed in 2D moiré superlattices [7–13]. However, their one-dimensional (1D) counterpart—the 1D moiré superlattice—has been rarely explored. On the other hand, a 1D heterostructure composed of a single-walled carbon nanotube (CNT) on top of hexagonal boron nitride (hBN) has recently exhibited many interesting physical phenomena [14–18], including a homogeneous Coulomb blockade [14], long-lifetime plasmons [16], and ultranarrow-linewidth photoluminescence [18], indicating an unprecedentedly high quality of the 1D heterostructure. We note that due to the 1.8% lattice mismatch a 1D moiré superlattice may appear in the CNT/hBN heterostructure, which is expected to alter the electronic bands as well as physical properties.

In this paper, we performed theoretical calculations of low-energy bands of 1D moiré superlattices composed of three representative types of single-walled CNTs on top of hBN substrate using a newly developed low-energy effective continuum model for 1D superlattices. The effective continuum model is constructed using long-wavelength components of the moiré superlattice potential, and we verify its validity by demonstrating that the calculated band structures agree well with those of the density functional theory (DFT) calculation. In the band structure calculation, we observed moiré-induced opening of small band gaps ranging from a few meV to a few tens of meV, which depends sensitively on the CNT chirality. The observed band-gap opening can be well understood within the effective continuum model.

II. THEORETICAL METHODS

A. Atomic structure

We consider a moiré superlattice system composed of a single-walled CNT on top of hBN. A single-walled CNT is a hollow cylindrical structure composed of a hexagonal lattice of carbon atoms. The hBN is a 2D hexagonal lattice of boron and nitrogen atoms. The bond length of hBN $a_{\text{B-N}}$ is $\sim$1.446 Å [19], which is 1.8% larger than the CNT's carbon-carbon bond length $a_{\text{C-C}} \sim 1.430$ Å. The distance between the bottom atoms of the CNT and hBN is set to be $d = 3.220$ Å, the same as the graphene/hBN superlattice case [15,20,21].

Rolling up a monolayer graphene sheet along different directions yields CNTs with different structures, which defines the chirality of the CNTs. Each CNT can be specified by a chiral vector $\mathbf{C}$ corresponding to the circumference of the CNT and a translation vector $\mathbf{T}$ being a primitive vector perpendicular to chiral vector $\mathbf{C}$. The chiral vector $\mathbf{C}$ can be described by a set of two integers (n, m), i.e., the chiral index of the CNT, such that $\mathbf{C} = n\mathbf{a}_1 + m\mathbf{a}_2$, where $\mathbf{a}_1$ and $\mathbf{a}_2$ are two primitive lattice vectors of monolayer graphene.

---

[*] These authors contributed equally to this work.
[†] wdluo@sjtu.edu.cn
[‡] zwshi@sjtu.edu.cn

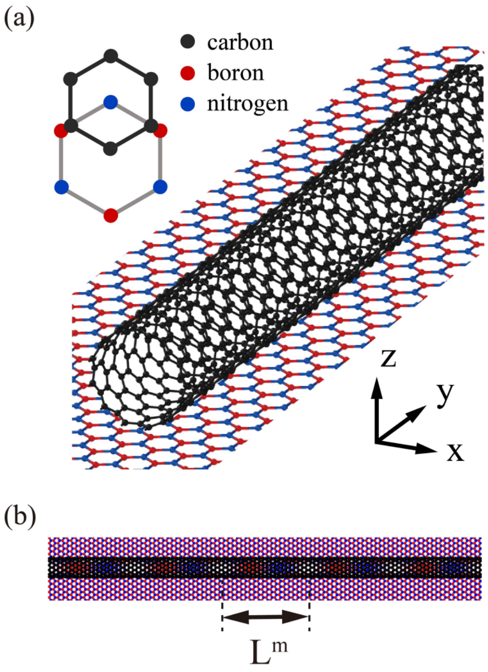

FIG. 1. (a) The perspective view of and (b) the moiré pattern of a single-walled carbon nanotube on top of a hBN substrate with an exaggerated lattice constant ratio for clarity. The inset in (a) shows the AB-stacking arrangement.

In this paper, we consider three representative types of CNTs, the (6, 6) armchair CNT (AC-CNT), the (9, 0) zigzag CNT (ZZ-CNT), and the (10, 0) ZZ-CNT on top of hBN.

The geometry of the CNT/hBN system is at zero twist angle, i.e., the bottom graphene hexagons of the CNT align perfectly with the hBN crystal with zero twist angle. The mismatch of the bond length between CNT and hBN results in the 1D moiré pattern, with the moiré period $|\mathbf{L}^{\mathrm{m}}|$ along the CNT direction. For the AC-CNT/hBN system, we have moiré period $|\mathbf{L}^{m}_{AC}| \approx 13.76$ nm, and for the ZZ-CNT/hBN system, we have moiré period $|\mathbf{L}^{m}_{ZZ}| \approx 23.86$ nm. Figure 1 shows the atomic structure and the 1D moiré interference pattern of CNT/hBN system with an exaggerated lattice constant ratio for clarity. We define the direction along CNT as the y direction and the direction perpendicular to CNT in the hBN plane as the x direction.

B. Density functional theory

In the DFT calculation, the superlattice system must have a definite unit cell, so we rationalize the relative bond length of CNT and hBN $a_{\text{B-N}}/a_{\text{C-C}} \sim 1.018$ to 56/55 [21]. This rationalization is not necessary in the effective continuum model that can deal with incommensurate superlattice systems [4].

DFT calculations are performed on the CNT/hBN moiré superlattice unit cell with the SIESTA *ab initio* package [22,23]. We use the local-density approximation [24] and norm-conserving pseudopotentials [25]. The moiré superlattice is constructed using a 56-unit supercell of the CNT and a 55-unit supercell of hBN. The width of the hBN substrate for a unit cell is 20 Å and the size of the out-of-plane direction was 50 Å to avoid fictitious interactions between periodically repeated unit cells. The wave functions are expanded using a double-zeta plus polarization basis with a cutoff of 80 Ry. The Gamma point is sampled in the Brillouin zone (BZ) to obtain the self-consistent charge density.

C. Effective continuum model for 1D superlattice

When the moiré period $|\mathbf{L}^{\mathrm{m}}|$ is much larger than the lattice constant in each layer, the interlayer interaction is dominated by long-wavelength components, allowing us to treat the problem in the effective continuum model which has been introduced for the twisted bilayer-graphene system [4], the graphene/hBN system [21], and the CNT/graphene system [26].

The effective continuum model uses the Bloch states in each layer as the basis to construct the effective Hamiltonian matrix, and the interaction between two layers mixes these Bloch states allowing interlayer tunneling, i.e., the nonzero off-diagonal terms in the Hamiltonian matrix. Here, we derive the low-energy effective continuum model for the CNT/hBN superlattice system following the similar approaches in previous studies [4,21,26].

A CNT can be viewed as a graphene nanoribbon plus the curvature effect. If neglecting the curvature effect, a CNT's wave function can be obtained by imposing the periodic boundary condition $\psi(\boldsymbol{r}) = \psi(\boldsymbol{r}+\boldsymbol{C})$ on the graphene's wave function, resulting in the quantization of crystal momentum perpendicular to the CNT direction $k_x = \frac{2\pi}{|\mathrm{C}|} j$, with j being an integer [27]. Hence the CNT's BZs are a set of parallel straight lines in the 2D graphene BZ.

For an (n, m) CNT, when the condition $n - m = 3N$ is satisfied, with N being an integer, the CNT's energy bands cross through the graphene's Dirac points ($\mathbf{K}$ and $\mathbf{K}'$ points) without a gap [27]. The typical interlayer tunneling strength between CNT and hBN is much weaker than the energy separation of minibands in CNT, so that we can truncate the low-energy Hilbert space to the subspace of the CNT's lowest minibands.

In the tight-binding description, the Hamiltonian of CNT near the $\mathbf{K}$ point is written as

$$H_{\mathrm{CNT}} \approx -\hbar v \mathbf{k} \cdot \boldsymbol{\sigma}, \tag{1}$$

where $v \approx 0.8 \times 10^6$ m/s is the Fermi velocity near the Dirac cone [28], $\mathbf{k}$ is the 1D relative wave vector of the CNT measured from the $\mathbf{K}$ point, and $\sigma = (\sigma_x, \sigma_y)$ is the Pauli matrix. The Hamiltonian of the CNT near the $\mathbf{K}'$ point can be obtained using the time-reversal symmetry.

The curvature of the tube modifies the band structure of CNTs [29–31]. Some metallic CNTs would be modified to small-gap semiconducting ones. The gap-opening of CNTs due to the curvature effect is expressed as $E_{gap} = \frac{t_g \pi^2}{8|C|^5}(n-m)(2n^2+5nm+2m^2)$ [29], where (n, m) is the chiral index of the CNT, t_g is the nearest-neighbor transfer integral of the CNT, and $|C|$ is the circumference of the CNT in units of $\sqrt{3}a_{\text{C-C}}$. When considering the curvature effect, the (N, N) AC-CNTs are still exactly metallic while the $(3N, 0)$ ZZ-CNTs start to have a small band gap.

In this paper, we calculate moiré band gaps for three representative types of CNTs with different original band gaps, i.e., metallic (N, N) AC-CNT with an exactly zero band gap,

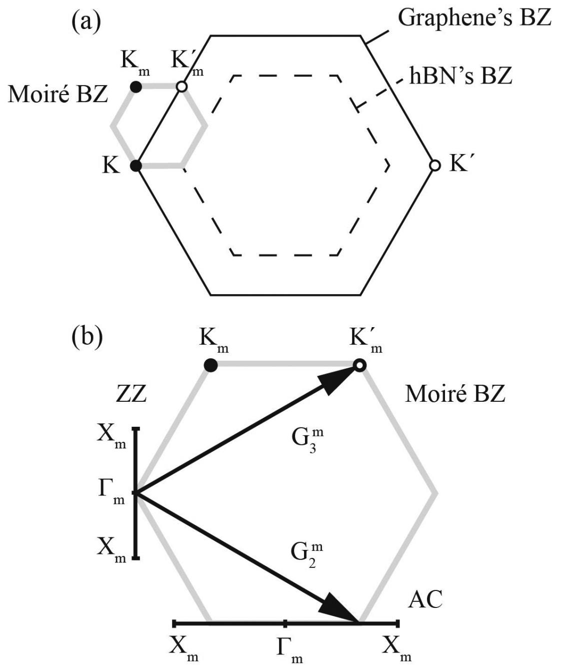

FIG. 2. (a) The BZ folding in graphene/hBN moiré superlattice, with an exaggerated lattice constant ratio for clarity. (b) The zoomed-in illustration of moiré BZ of AC-CNT/hBN and ZZ-CNT/hBN systems.

metallic $(3N, 0)$ ZZ-CNT with a small band gap, and semiconducting ZZ-CNT with a large band gap.

The low-energy effective Hamiltonian of hBN consists of a kinetic off-diagonal term similar to that of graphene around its Dirac points and extra diagonal on-site potential terms. This Hamiltonian yields a massive Dirac cone separated by an energy gap $|V_B - V_N|$, with a quadratic energy dispersion. Since the band gap of hBN ($\sim$5 eV) is very large, in the low-energy region, we can safely neglect the dispersion by retaining only the diagonal potential term in the Hamiltonian [32], i.e.,

$$H_{\text{hBN}} \approx \begin{pmatrix} V_{\text{N}} & 0 \\ 0 & V_{\text{B}} \end{pmatrix}, \tag{2}$$

where $V_{\text{N}} = -1.4$ eV and $V_{\text{B}} = 3.34$ eV are the on-site potentials of nitrogen and boron atoms, respectively.

When the CNT is on top of hBN, the two layers interact and the CNT's BZ folds into the 1D moiré BZ. Figure 2 illustrates the BZ and miniband folding in the CNT/hBN moiré superlattice with an exaggerated lattice constant ratio for clarity, where the solid black and dotted black hexagons are auxiliary graphene's and hBN's BZs, and $\mathbf{G}_2^m$ and $\mathbf{G}_3^m$ are two superlattice reciprocal lattice vectors in the graphene/hBN system. The 1D reciprocal lattice vector can be represented as $\mathbf{G}_{AC}^m = \frac{1}{2}(\mathbf{G}_2^m + \mathbf{G}_3^m)$ for AC-CNT/hBN and $\mathbf{G}_{ZZ}^m = \frac{1}{2}(\mathbf{G}_2^m - \mathbf{G}_3^m)$ for ZZ-CNT/hBN.

The interlayer tunneling matrix has the same form as the case of CNT/graphene system with $\theta = 0^\circ$ rotation, and the tunneling matrix $T_{\mathbf{q},k_y}$ describing a process in which a Bloch electron in one valley with momentum k_y of the CNT hops to a Bloch state in the same valley with momentum $\mathbf{q}$ of the hBN is written as [21,26]

$$T_{\mathbf{q},k_y} = \frac{t}{\sqrt{2\pi}} \sum_{j=1}^{3} T_j \exp\left[-\frac{R^2}{2}\left(q_x - G_{jx}^m\right)^2\right] \delta_{q_y - k_y, G_{jy}^m}, \tag{3}$$

where $\mathbf{q}$ and k_y are the wave vectors measured from the same CNT Dirac point, $t \equiv t(k_D)$ is the in-plane Fourier transform of the transfer integral $t(\vec{r})$ [4], k_D is the magnitude of reciprocal vector of Dirac point in CNT, $\mathbf{G}_1^m = 0$, $\mathbf{G}_2^m$ and $\mathbf{G}_3^m$ are two vectors depicted in Fig. 2, R is the radius of CNT, and T_j are the tunneling matrices of $\mathbf{G}_j^m$ with $T_1 = \left(\begin{smallmatrix} 1 & 1 \\ 1 & 1 \end{smallmatrix}\right)$, $T_2 = \left(\begin{smallmatrix} e^{-i\phi} & 1 \\ e^{i\phi} & e^{-i\phi} \end{smallmatrix}\right)$, $T_3 = \left(\begin{smallmatrix} e^{i\phi} & 1 \\ e^{-i\phi} & e^{i\phi} \end{smallmatrix}\right)$, and $\phi = 2/3\pi$. Higher-order tunneling, such as $t(2k_D)$, is much smaller than the first-order $t(k_D)$, and thus can be safely neglected [33].

From Eq. (3), we see that the moiré potential couples the Bloch states in CNT and those in hBN, and therefore allows tunneling. In the tunneling process, the crystal momentum along the CNT direction (k_y direction) is conserved which is similar to the case in 2D moiré superlattice systems, while the crystal momentum perpendicular to the CNT direction (k_x direction) does not have to be conserved because there is no translation symmetry along this direction. We denote these matrices with $k_x \neq G_{jx}^m$ as the vertical tunneling $T_j^\perp$.

In the k-space representation, the Hamiltonian matrix can be written at discrete k points $\mathbf{k} = \mathbf{k_0} + n\mathbf{G}_{AC}^m$ for AC-CNT/hBN and $\mathbf{k} = \mathbf{k_0} + n\mathbf{G}_{ZZ}^m$ for ZZ-CNT/hBN, where $\mathbf{k_0}$ is a vector defined within the one-dimensional moiré BZ, and $k_0 = 0$ corresponds to the Γ_m point. We choose sufficient k points to diagonalize the Hamiltonian. Due to the vertical tunneling $T_j^\perp$, a Bloch electron at $\mathbf{k}$ in CNT can tunnel to many hBN states with wave vectors perpendicular to it. In order to improve the calculation efficiency, when constructing the total Hamiltonian matrix, we only allow the CNT state at $\mathbf{k}$ to tunnel to three representative hBN states at $\mathbf{q} = \mathbf{k} + \mathbf{G}_j^m$ with $j = 1$, 2, and 3, and use the result of DFT to fit the band gaps. The dimension of the Hamiltonian matrix in the effective continuum model is roughly 10^2, and the diagonalization is much faster than that in DFT, which is similar to the 2D case [34].

III. RESULTS AND DISCUSSION

A. Band-gap opening in a metallic (6, 6) AC-CNT/hBN moiré superlattice

First, we calculate the band structure of a (6, 6) AC-CNT/hBN moiré superlattice using both DFT and the effective continuum model. Figures 3(a) and 3(b) compare the electronic band structures calculated by the two methods on the k-space path shown in Fig. 2(b). The origin of the energy axis is reset to the charge neutral point in all the calculations in this paper. From Fig. 3, we see that the results of two methods are consistent. Figures 3(c) and 3(d) describe two tunneling processes accounting for the gap opening g_1 and g_2 at two high-symmetry points denoted by dashed circles in Fig. 3(b), respectively, which provide an intuitive understanding of the moiré-induced opening of band gaps.

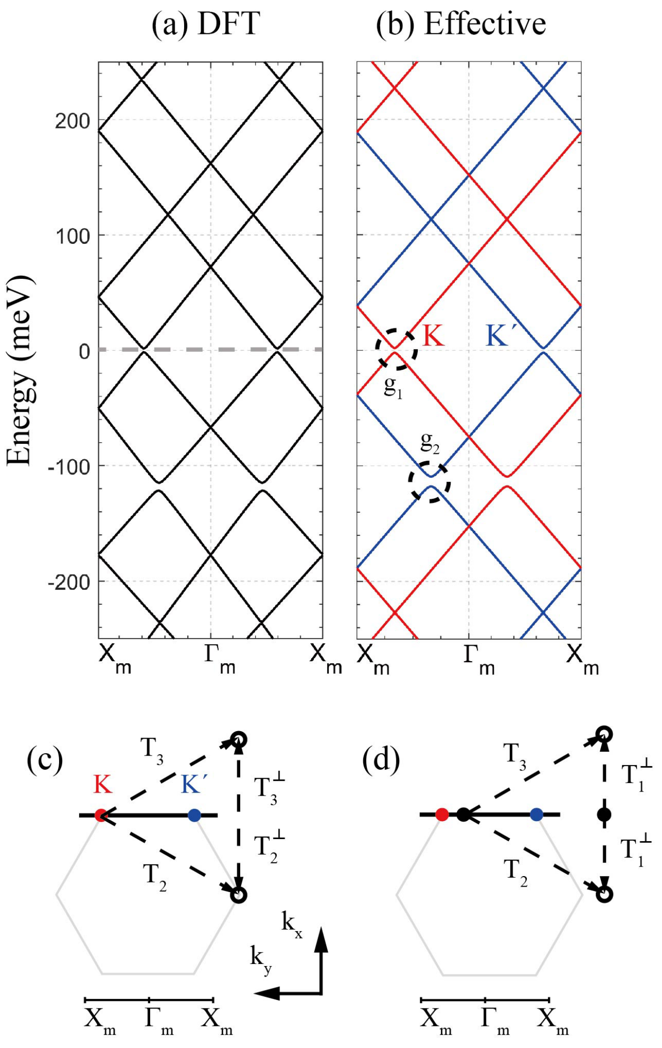

FIG. 3. Band structures of a (6, 6) AC-CNT/hBN system calculated by (a) DFT, and (b) the effective continuum model on the *k*-space path shown in Fig. 2(b). Two tunneling processes accounting for (c) gap opening g_1 and (d) gap opening g_2 denoted by dashed circles in (b), where the solid black dots denote the CNT states, the hollow black dots denote the hBN states, and the dashed arrows stand for the tunneling process.

Comparing the electronic bands in Figs. 3(a) and 3(b), we recognize that two sets of identical band structures come from two valleys of the (6, 6) AC-CNT, which are colored by red and blue in Fig. 3(b). We also find that the band gaps only appear at the crossing points of bands with the same color (the same valley). It is because the intervalley tunneling component, i.e., the short-wavelength component of the moiré potential is negligible, and thus the valley-index remains a good quantum number.

A (6, 6) AC-CNT should remain exactly metallic with zero band gap even if considering curvature effect. Therefore, the tiny band gap g_1 at the original Dirac point about 3 meV in DFT is purely caused by the moiré potential. In the effective continuum model, this band gap g_1 can be captured by a tunneling process shown in Fig. 3(c), and the effective Hamiltonian of the system truncated in the first moiré BZ is

$$H_{g_1} = \begin{pmatrix} H_{CNT} & T_2^\dagger + T_3^{\perp\dagger} & T_2^{\perp\dagger} + T_3^\dagger \\ T_2 + T_3^\perp & H_{\mathrm{hBN}} & 0 \\ T_2^\perp + T_3 & 0 & H_{\mathrm{hBN}} \end{pmatrix}, \tag{4}$$

where H_{CNT} is the Hamiltonian of AC-CNT at Dirac point, H_{hBN} is the Hamiltonian of hBN, the off-diagonal terms are interlayer tunneling matrices, and $T_j^\perp$ stands for vertical tunneling of T_j. At the original Dirac point, two tunneling processes T_2 and T_3 mix with each other because of the vertical tunneling, and open a tiny gap g_1 of ~3 meV.

At the first-order superlattice Dirac point, the band splitting is larger in the hole side (~6 meV) in DFT, while it is much narrower in the electron side (<1 meV). The same result appears in our effective continuum model. This electron-hole asymmetry is consistent with previous results of the 2D graphene/hBN moiré system [21]. We further find that if we artificially exchange the ratio of bond length between carbon-carbon bonds and nitrogen-boron bonds, i.e., $a_{\text{B-N}}/a_{\text{C-C}} = 56/55$, the electron-hole asymmetry will reverse accordingly, indicating that the electron-hole asymmetry is relevant to the lattice mismatch. In the effective continuum model, the splitting g_2 at the first-order superlattice Dirac point can be captured by a hBN-mediated tunneling process as shown in Fig. 3(d), where the Hamiltonian of the system truncated in the first moiré BZ is

$$H_{g_2} = \begin{pmatrix} H_{CNT} & 0 & T_2^\dagger & T_3^\dagger \\ 0 & H_{CNT} & T_1^{\perp\dagger} & T_1^{\perp\dagger} \\ T_2 & T_1^\perp & H_{\mathrm{hBN}} & 0 \\ T_3 & T_1^\perp & 0 & H_{\mathrm{hBN}} \end{pmatrix}, \tag{5}$$

where H_{CNT} is the Hamiltonian of AC-CNT at the first-order superlattice Dirac point in the moiré BZ. Two AC-CNT quantum states with the same energy tunnel to two hBN states. This tunneling mixes the Hilbert space of these two CNT states and causes band anticrossing.

B. Band-gap opening in a small-band-gap (9, 0) ZZ-CNT/hBN moiré superlattice

We also calculate band structure of a (9, 0) ZZ-CNT/hBN moiré superlattice. Figures 4(a) and 4(b) compare the electronic band structure calculated by two methods on the *k*-space path shown in Fig. 2(b). From Fig. 4, we can see that the results of these two methods are consistent. Figures 4(c) and 4(d) describe the tunneling processes accounting for the gap opening g_1 at the X_m point and g_2 at the Γ_m point of the moiré BZ, respectively, in the effective continuum model.

In Fig. 4(a), the result calculated by DFT, we see two sets of band structures with a tiny split (~2 meV) originated from **K** and **K**′ valleys of the (9, 0) ZZ-CNT, while in Fig. 4(b), the degeneracy of two valleys is not broken in the effective continuum model. This split is due to the breaking of rotation symmetry around the axis of CNTs caused by the hBN substrate, which is not included in the effective continuum model. Although the valley degeneracy is broken, the valley index remains a good quantum number due to negligible intervalley coupling.

From Fig. 4, we see that band gaps appear in the band structure of the ZZ-CNT/hBN system at the Dirac point, the

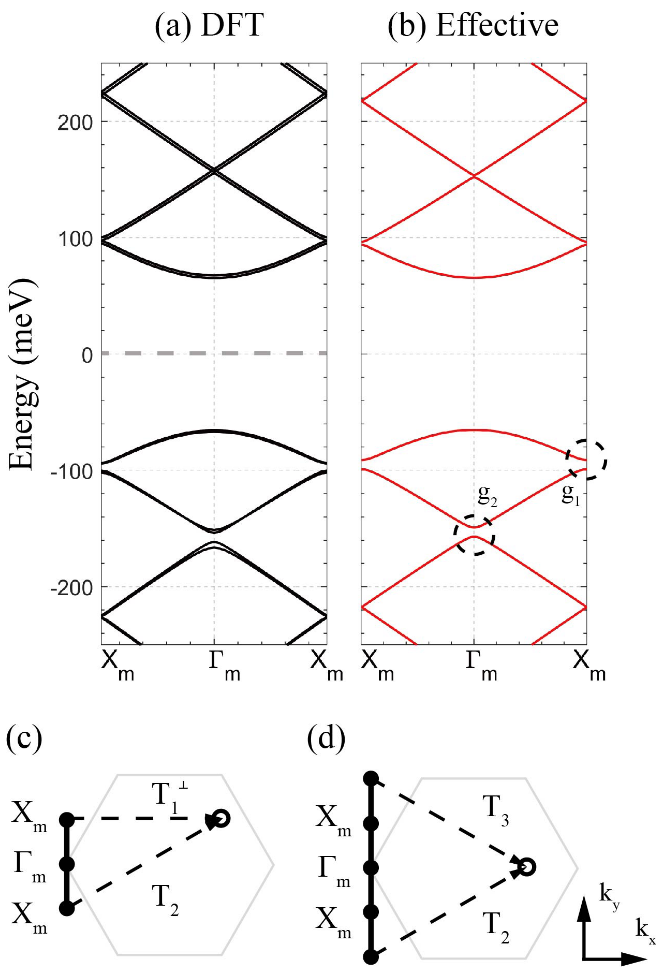

FIG. 4. Band structures of a (9, 0) ZZ-CNT/hBN system calculated by (a) DFT and (b) the effective continuum model on the *k*-space path shown in Fig. 2(b). Two tunneling processes accounting for (c) gap opening g_1 and (d) gap opening g_2 denoted by dashed circles in (b), where the solid black dots denote the CNT states, the hollow black dots denote the hBN states, and the dashed arrows stand for the tunneling process.

zone boundary, and between the second and the third band within one valley. A (9, 0) ZZ-CNT originally opens a band gap of 140 meV at its Dirac point due to the curvature effect. The moiré potential slightly shrink this band gap to 130 meV.

At the zone boundary X_m, a band splitting within one valley appears between the first and the second hole (electron) bands. The splitting is large in the hole side, about 6 meV for one valley and 8 meV for the other valley in DFT, and it is narrower in the electron side as shown in Fig. 4(a). In the effective continuum model, the splitting g_1 at the zone boundary X_m can be captured by a hBN-mediated tunneling process as shown in Fig. 4(d), where the Hamiltonian of the system truncated in the first moiré BZ is

$$H_{g_1} = \begin{pmatrix} H_{CNT} & 0 & T_1^{\perp\dagger} \\ 0 & H_{CNT} & T_2^{\dagger} \\ T_1^{\perp} & T_2 & H_{\mathrm{hBN}} \end{pmatrix}, \tag{6}$$

where H_{CNT} is the Hamiltonian of ZZ-CNT at the moiré BZ boundary. Two CNT quantum states with the same energy tunneling to the same hBN state causes band anticrossing at the zone boundary, which also explains the BZ folding in the ZZ-CNT/hBN moiré superlattice system.

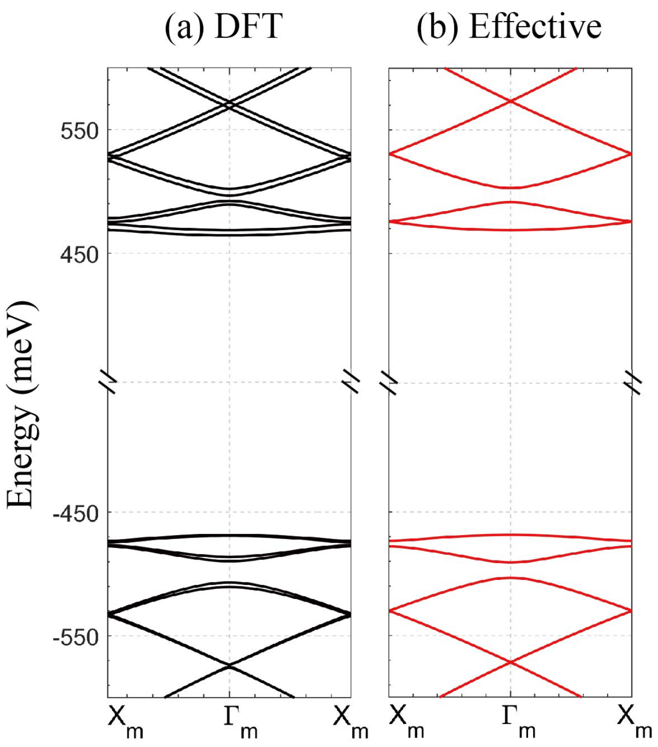

FIG. 5. Band structures of a (10, 0) ZZ-CNT/hBN system calculated by (a) DFT and (b) the effective continuum model.

The band gap g_2 at Γ_m shares features similar to the one at the zone boundary, and the tunneling process which causes the splitting is shown in Fig. 4(d). The band structure of ZZ-CNT/hBN also shows electron-hole asymmetry as discussed in the armchair case.

C. Band-gap opening in a semiconducting (10, 0) ZZ-CNT/hBN moiré superlattice

The band structure of a semiconducting (10, 0) ZZ-CNT/hBN moiré superlattice is also calculated. Figures 5(a) and 5(b) compare the electronic band structure calculated by two methods on the *k*-space path shown in Fig. 2(b). The splitting of two valleys and the band-gap opening (∼20 meV at Γ_m, ∼5 meV at X_m) in this system is similar to the (9, 0) ZZ-CNT/hBN system.

The original band gap of the (10, 0) ZZ-CNT at Γ is 0.94 eV, and is slightly shrinked to 0.93 eV by the moiré potential based on the DFT calculations. This feature is consistent with the previous study on substrate-induced band-gap renormalization in the (10, 0) ZZ-CNT/hBN system [15].

From Fig. 3, Fig. 4, and Fig. 5, we find that there is a positive correlation between the superlattice band gap and the original CNT band gap. When the original band gap is large, the superlattice band gap is also large. This can be explained by the overlap of spinor states in the CNT [35]. If the original band gap of the CNT is large, the overlap of two spinor states in the CNT connected by a 1D reciprocal lattice vector is also large. In an extreme case, when the original band gap in the CNT is exactly zero, i.e., the (N, N) AC-CNT case, the overlap of two spinor states connected by $\mathbf{G}_{AC}^{m}$ is zero. As a result, the moiré-induced gap is the smallest [Figs. 3(a) and 3(b)]. Note that the nonzero moiré gap for the AC-CNT case can only originate from a hBN-mediated tunneling process.

IV. CONCLUSION

We have calculated the electronic band structure of 1D moiré superlattices of three representative CNTs on top of hBN using a newly developed effective continuum model for 1D superlattice. The effective model provides a simple and appealing physical interpretation of the band structure of the moiré system and can be easily extended to other 1D/2D moiré superlattice systems. We observe moiré-induced opening of small band gaps ranging from a few meV to a few tens of meV, which depends sensitively on the CNT chirality. The results have been confirmed by DFT calculations. Additionally, the opening of moiré gaps can be understood intuitively from the coupling between CNT states and hBN states within the effective continuum model. The predicted moiré gaps should have an effect on the electron transport as well as the electronic transitions, and thus can be experimentally verified by electrical transport and optical spectroscopy measurements.

ACKNOWLEDGMENTS

This work is supported by the open research fund of Songshan Lake Materials Laboratory (Grant No. 2021SLABFK07), National Natural Science Foundation of China (Grants No. 11774224, No. 12074244, No. 11521404, and No. 11774278), SJTU (Grant No. 21X010200846), and "Shuguang Program" supported by Shanghai Education Development Foundation and Shanghai Municipal Education Commission. The computations in this paper were run on the π 2.0 cluster supported by the Center for High Performance Computing at Shanghai Jiao Tong University.

---

[1] J. M. B. Lopes dos Santos, N. M. R. Peres, and A. H. Castro Neto, Phys. Rev. Lett. **99**, 256802 (2007).

[2] S. Carr, D. Massatt, S. Fang, P. Cazeaux, M. Luskin, and E. Kaxiras, Phys. Rev. B **95**, 075420 (2017).

[3] E. Suárez Morell, J. D. Correa, P. Vargas, M. Pacheco, and Z. Barticevic, Phys. Rev. B **82**, 121407(R) (2010).

[4] R. Bistritzer and A. H. MacDonald, Proc. Natl. Acad. Sci. USA **108**, 12233 (2011).

[5] N. N. T. Nam and M. Koshino, Phys. Rev. B **96**, 075311 (2017).

[6] G. Trambly de Laissardière, D. Mayou, and L. Magaud, Nano Lett. **10**, 804 (2010).

[7] E. C. Regan, D. Wang, C. Jin, M. I. Bakti Utama, B. Gao, X. Wei, S. Zhao, W. Zhao, Z. Zhang, K. Yumigeta, M. Blei, J. D. Carlström, K. Watanabe, T. Taniguchi, S. Tongay, M. Crommie, A. Zettl, and F. Wang, Nature (London) **579**, 359 (2020).

[8] B. Padhi, R. Chitra, and P. W. Phillips, Phys. Rev. B **103**, 125146 (2021).

[9] Y. Cao, V. Fatemi, A. Demir, S. Fang, S. L. Tomarken, J. Y. Luo, J. D. Sanchez-Yamagishi, K. Watanabe, T. Taniguchi, E. Kaxiras, R. C. Ashoori, and P. Jarillo-Herrero, Nature (London) **556**, 80 (2018).

[10] Y. Cao, V. Fatemi, S. Fang, K. Watanabe, T. Taniguchi, E. Kaxiras, and P. Jarillo-Herrero, Nature (London) **556**, 43 (2018).

[11] G. Chen, L. Jiang, S. Wu, B. Lyu, H. Li, B. L. Chittari, K. Watanabe, T. Taniguchi, Z. Shi, J. Jung, Y. Zhang, and F. Wang, Nat. Phys. **15**, 237 (2019).

[12] G. Chen, A. L. Sharpe, P. Gallagher, I. T. Rosen, E. J. Fox, L. Jiang, B. Lyu, H. Li, K. Watanabe, T. Taniguchi, J. Jung, Z. Shi, D. Goldhaber-Gordon, Y. Zhang, and F. Wang, Nature (London) **572**, 215 (2019).

[13] M. Yankowitz, S. Chen, H. Polshyn, Y. Zhang, K. Watanabe, T. Taniguchi, D. Graf, A. F. Young, and C. R. Dean, Science **363**, 1059 (2019).

[14] A. Baumgartner, G. Abulizi, K. Watanabe, T. Taniguchi, J. Gramich, and C. Schönenberger, Appl. Phys. Lett. **105**, 023111 (2014).

[15] N. A. Lanzillo, N. Kharche, and S. K. Nayak, Sci. Rep. **4**, 3609 (2014).

[16] Z. Shi, X. Hong, H. A. Bechtel, B. Zeng, M. C. Martin, K. Watanabe, T. Taniguchi, Y.-R. Shen, and F. Wang, Nat. Photonics **9**, 515 (2015).

[17] Q. Gao, J. Chen, B. Lyu, A. Deng, L. Wang, T. Wu, K. Watanabe, T. Taniguchi, and Z. Shi, Appl. Phys. Lett. **117**, 023101 (2020).

[18] N. Fang, K. Otsuka, A. Ishii, T. Taniguchi, K. Watanabe, K. Nagashio, and Y. K. Kato, ACS Photonics **7**, 1773 (2020).

[19] L. Liu, Y. P. Feng, and Z. X. Shen, Phys. Rev. B **68**, 104102 (2003).

[20] G. Giovannetti, P. A. Khomyakov, G. Brocks, P. J. Kelly, and J. van den Brink, Phys. Rev. B **76**, 073103 (2007).

[21] P. Moon and M. Koshino, Phys. Rev. B **90**, 155406 (2014).

[22] D. Sánchez-Portal, P. Ordejon, E. Artacho, and J. M. Soler, Int. J. Quantum Chem. **65**, 453 (1997).

[23] J. M. Soler, E. Artacho, J. D. Gale, A. García, J. Junquera, P. Ordejón, and D. Sánchez-Portal, J. Phys.: Condens. Matter **14**, 2745 (2002).

[24] D. M. Ceperley and B. J. Alder, Phys. Rev. Lett. **45**, 566 (1980).

[25] N. Troullier and J. L. Martins, Phys. Rev. B **43**, 8861 (1991).

[26] B. Flebus and A. H. MacDonald, Phys. Rev. Research **2**, 022041(R) (2020).

[27] T. Ando, J. Phys. Soc. Jpn. **74**, 777 (2005).

[28] P. Moon and M. Koshino, Phys. Rev. B **87**, 205404 (2013).

[29] A. Kleiner and S. Eggert, Phys. Rev. B **63**, 073408 (2001).

[30] A. Kleiner and S. Eggert, Phys. Rev. B **64**, 113402 (2001).

[31] S. Reich, C. Thomsen, and P. Ordejón, Phys. Rev. B **65**, 155411 (2002).

[32] M. Kindermann, B. Uchoa, and D. L. Miller, Phys. Rev. B **86**, 115415 (2012).

[33] M. Koshino, New J. Phys. **17**, 015014 (2015).

[34] F. S. Carr Stephen and K. Efthimios, Nat. Rev. Mater. **5**, 748 (2020).

[35] P. L. McEuen, M. Bockrath, D. H. Cobden, Y.-G. Yoon, and S. G. Louie, Phys. Rev. Lett. **83**, 5098 (1999).